Research Article

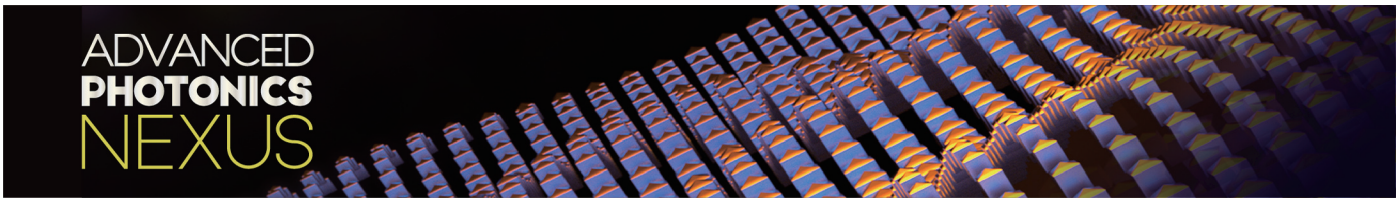


# Mapping ultrafast timing jitter in dispersion-managed 89 GHz frequency microcombs via self-heterodyne linear interferometry

Wenting Wang,[a,b,†] Wenzheng Liu,[a,*,†] Hao Liu,[a,†] Tristan Melton,[a] Alwaleed Aldhafeeri,[a] Dong-Il Lee,[a] Jinghui Yang,[a] Abhinav Kumar Vinod,[a] Jinkang Lim,[a] Yoon-Soo Jang,[a] Heng Zhou,[c] Mingbin Yu,[d,e] Patrick Guo-Qiang Lo,[d,f] Dim-Lee Kwong,[d] Peter DeVore,[g] Jason Chou,[g] Ninghua Zhu,[h] and Chee Wei Wong[a,*]

[a]University of California Los Angeles, Fang Lu Mesoscopic Optics and Quantum Electronics Laboratory, Los Angeles, California, United States
[b]Beijing Institute of Technology, School of Optics and Photonics, Mesoscopic Optics and Advanced Instruments Laboratory, Beijing, China
[c]University of Electronic Science and Technology of China, Key Lab of Optical Fiber Sensing and Communication Networks, Chengdu, China
[d]Institute of Microelectronics, A*STAR, Singapore
[e]Shanghai Institute of Microsystem and Information Technology, Shanghai Industrial Technology Research Institute, State Key Laboratory of Functional Materials for Informatics, Shanghai, China
[f]Advanced Micro Foundry, Singapore
[g]Lawrence Livermore National Laboratory, Livermore, California, United States
[h]Nankai University, Institute of Intelligent Photonics, Tianjin, China

**Abstract.** Laser frequency microcombs provide a series of equidistant, coherent frequency markers across a broad spectrum, enabling advancements in laser spectroscopy, dense optical communications, precision distance metrology, and astronomy. Here, we design and fabricate silicon nitride, dispersion-managed microresonators that effectively suppress avoided-mode crossings and achieve close-to-zero averaged dispersion. Both the stochastic noise and mode-locking dynamics of the resonator are numerically and experimentally investigated. First, we experimentally demonstrate thermally stabilized microcomb formation in the microresonator across different mode-locked states, showing negligible center frequency shifts and a broad frequency bandwidth. Next, we characterize the femtosecond timing jitter of the microcombs, supported by precise metrology of the timing phase and relative intensity noise. For the single-soliton state, we report a relative intensity noise of −153.2 dB/Hz, close to the shot-noise limit, and a quantum-noise–limited timing jitter power spectral density of 0.4 as$^2$/Hz at a 100 kHz offset frequency, measured using a self-heterodyne linear interferometer. In addition, we achieve an integrated timing jitter of 1.7 fs $\pm$ 0.07 fs, measured from 10 kHz to 1 MHz. Measuring and understanding these fundamental noise parameters in high clock rate frequency microcombs is critical for advancing soliton physics and enabling new applications in precision metrology.

Keywords: frequency microcomb; timing jitter; self-heterodyne linear interferometry; dispersion-managed microresonator.

Received Dec. 18, 2024; revised manuscript received Jan. 24, 2025; accepted for publication Apr. 8, 2025; published online May 9, 2025.

© The Authors. Published by SPIE and CLP under a Creative Commons Attribution 4.0 International License. Distribution or reproduction of this work in whole or in part requires full attribution of the original publication, including its DOI.

[DOI: 10.1117/1.APN.4.3.036011]

## 1 Introduction

Laser frequency combs have impacted science and technology fields with their equidistant frequency spacings, serving as unique coherent clockwork.[1,2] Recent emerging applications include, for example, clocks for space-borne networks,[3,4] precise laser ranging metrology for autonomous platforms,[5] and low-phase noise radio frequency generation,[6,7] all aided by low timing jitter mode-locked frequency combs. The observations of dissipative soliton microcombs in single microresonators[8,9] or coupled microresonators[10] with smooth spectral profiles and dispersive waves[11] offer opportunities to examine soliton comb

*Address all correspondence to Wenzheng Liu, wzliu@g.ucla.edu; Chee Wei Wong, cheewei.wong@ucla.edu

†These authors contributed equally to this work.

dynamics in miniature platforms. There has been significant progress in soliton microcomb formation in different integrated microresonator platforms such as $Si_3N_4$,[12] AlN,[13] $LiNbO_3$,[14] and AlGaAs,[15] benefiting from either ultrahigh quality factors or large nonlinear coefficients. The recent demonstrations of electrically pumped turn-key soliton microcombs[16–18] and mode-locked microcombs[19] further reinforce the viability of the fully integrated frequency microcomb and pave the way for integrated functionalities such as terabit-per-second coherent transceivers,[20–22] parallel coherent LiDAR,[23] astrophysical spectrographs,[24,25] laser spectroscopy,[26–28] distance ranging,[29–31] low-noise microwave generation,[32–34] and convolutional processing networks.[35,36]

In soliton microcombs, the pump-resonance detuning noise[37] plays a critical role in the pump-to-repetition–rate noise transduction.[38–40] A low repetition-rate phase noise (repetition-rate timing jitter) regime exists at a detuning where the soliton center frequency shift from dispersive-wave emission is balanced by nonlinear effects. The phase noise can be improved by injecting the locked pump laser into resonant cavities,[19] by pumping the microresonators with a narrow linewidth laser,[41] by optimizing high-order dispersion of the microresonators,[42] and by thermal stabilization with an auxiliary laser.[43] Quantum motion of the microresonators has also been observed recently through timing jitter characterization in counterpropagating soliton pairs after suppressing common-mode technical noise.[44] With close-to-zero net group velocity dispersion (GVD), dispersion-managed soliton microcombs have been theoretically and experimentally investigated in active resonators featuring shorter pulse widths as well as better timing stability.[44–46] Therefore, the precise characterization of timing jitter in various microcombs is highly demanded. Direct photon detection can characterize timing jitter when repetition rates are detectable, but it has a limited timing jitter power spectral density (PSD) noise floor of $1 \times 10^{-6}$ $\mathrm{fs}^2/\mathrm{Hz}$ at 1 MHz offset frequency.[12] It is sensitive to intensity-noise-to-phase-noise (IM-PM) conversion.[47] Linear fiber interferometry[34,48] could provide a lower timing jitter PSD noise floor of $1 \times 10^{-9}$ $\mathrm{fs}^2/\mathrm{Hz}$, which is free of the IM-PM conversion and shot-noise limit.

Here, we demonstrated a series of thermally intracavity power-stabilized microcombs at different mode-locked states in 89 GHz dispersion-managed $Si_3N_4$ microresonators with negligible center frequency shifts and a broad frequency bandwidth. The demonstrated dispersion-managed (DM) microcombs not only expand the scope of soliton dynamics[8–11] but also enable low-jitter soliton trains. The DM microcombs suppressed occurrences of avoided-mode crossings (AMX),[49–51] compared with constant-dispersion microcombs, allowing lower timing jitter PSDs. Subsequently, we determine the intensity and timing fluctuations of the soliton microcombs at the single-soliton, multiple-soliton, and soliton crystal[52] states. As microcomb oscillators have high repetition rates, low pulse energy, and high pulse background, we present a linear interferometry approach with tens of zeptosecond/$\mathrm{Hz}^{1/2}$ timing jitter resolution to characterize its jitter. We note that the approach in Refs. 34 and 48 is reference-free and independent of the repetition rate, expanding from prior silica microcomb[34] and fiber comb studies[48] to the 89 GHz pulse train timing jitter measurements of the silicon nitride DM microcombs. The measurement of the fundamental timing jitter is based on (1) time delay for the frequency discrimination and (2) optical carrier interference for optical phase discrimination. We observe a relative intensity noise (RIN) of $-153.2$ dB/Hz at 100 kHz offset, with a corresponding integrated RIN of 0.034% from 100 Hz to 10 MHz for the single-soliton microcomb. For the single-soliton microcomb, the quantum-noise–limited timing jitter PSD is determined as 0.4 $\mathrm{as}^2/\mathrm{Hz}$ for 100 kHz offset, with an integrated jitter of 1.7 fs $\pm$ 0.07 fs from 10 kHz to 1 MHz. The integrated timing jitter from 10 kHz to 44.5 GHz Nyquist is ≈32.3 fs.

## 2 Methods

### 2.1 Dispersion-Managed Microresonator Fabrication

The fabrication procedure of the microresonator starts with a 3 $\mu$m thick $SiO_2$ layer that is first deposited via plasma-enhanced chemical vapor deposition (PECVD) on a $p$-type 8″ silicon wafer to serve as the undercladding oxide. An 800 nm silicon nitride is subsequently deposited via low-pressure chemical vapor deposition (LPCVD), and the resulting nitride layer is patterned by optimized 248 nm deep-ultraviolet lithography and etched down to the buried oxide cladding via an optimized reactive ion etch. The nitride microresonators are then overcladded with a 3 $\mu$m thick oxide layer, deposited initially with LPCVD for 0.5 $\mu$m and then with PECVD for 2.5 $\mu$m.

### 2.2 Dispersion-Managed Microcomb Formation Numerical Simulation and Stochastic Noise Calculation

After taking anomalous GVD and AMX into consideration, we have implemented the Ikeda method to obtain the roundtrip-varying nonmean-field microcomb dynamics and noise character written as

$$\begin{cases} E_{m+1}(0,t) = \sqrt{T_c}E_{\mathrm{in}} + \sqrt{1-T_c}e^{-i(\omega_0-\omega_p)t_R}E_m(L_{\mathrm{cav}},t) \\ \frac{\partial \tilde{E}_m(z,\omega)}{\partial z} = -\left[\alpha - i\frac{\beta_2(z)}{2}\omega^2\right]\tilde{E}_m(z,\omega) + i\gamma(z)\tilde{E}_m(z,\omega) \star \{\mathcal{F}[R(t')] \\ \qquad \times \mathcal{F}[|E_m(z,t)|^2]\}, \end{cases}$$

where $t_R$ is the roundtrip time, $z$ is the propagation distance within each cavity round trip, $t$ is the fast time, $E_m(z,t)$ is the intracavity electric field of the $m$'th roundtrip, the Fourier transform correspondence on the fast time is $\tilde{E}_m(z,\omega)$, $E_{\mathrm{in}}$ is the external pump field, $\alpha$ is the propagation loss, $T_c$ is the coupling strength, $L_{\mathrm{cav}}$ is the cavity length, $\delta = (\omega_0 - \omega_p)t_R$ is the pump-resonance detuning phase, and $\beta_2(z)$ is the second-order dispersion coefficient varying over the roundtrip position. Here, $\beta_2(z)$ is chosen from Fig. 1(b) ensuring the averaged $\beta_2$ is $-4.3$ $\mathrm{fs}^2/\mathrm{mm}$, based on our experimental characterization. $\gamma(z)$ is the Kerr nonlinear coefficient varying over the roundtrip position. $R(t)$ is the nonlinear response function, including the Raman response function. To incorporate the avoided-mode crossing-induced frequency shift, an additional frequency shift $\Delta_n$ is introduced to the $n$'th mode so that the mode frequency becomes $\omega_n = \omega_0 + D_1 n + \frac{D_2 n^2}{2} + \Delta_n$. $\Delta_n$ is determined by the empirical two-parameter model $\frac{\Delta_n}{2\pi} = \frac{-a/2}{n-b-0.5}$, where $a$ is the maximum mode frequency shift and $n$ and $b$ are the mode number and mode number for the maximum mode frequency shift, respectively. The thermal effect is not considered in the simulation because of the dual-driven thermal balance and the thermoelectric cooler (TEC) module. From the cavity-mode dispersion characterization, the cavity-free spectral range $D_1/2\pi = 88.52$ GHz. Furthermore, we estimate the maximum

frequency shift to be $\frac{\Delta_\mu}{2\pi} = 130$ MHz at 1581.5 nm determined by the spectral peak in the soliton microcomb optical spectrum. The estimated value is supported by comparing the simulated comb spectrum with the experimental result, which is in good qualitative agreement. A total of 2000 modes centered at the pump are incorporated into the model. The simulation starts with vacuum noise and runs for $1 \times 10^5$ roundtrips until the solution reaches a steady state.

To characterize the performance of the timing jitter, we introduced the thermal noise $\epsilon_\Theta$, shot noise $\epsilon_s$, pumping laser's intensity noise $\epsilon_{\text{in}}$, and frequency noise $\epsilon_\omega$ into our modeling. The dynamics can be represented as

$$\begin{cases} E_{m+1}(0,t) = \sqrt{T_c}(E_{\text{in}+}\epsilon_{\text{in}}) + \sqrt{1-T_c}e^{-i(\omega_0-\omega_{p-}\epsilon_\omega)t_R} \\ \qquad E_m(L_{\text{cav}},t) + \epsilon_{\text{s}} \\ \frac{\partial \tilde{E}_m(z,\omega)}{\partial z} = -\left[\alpha - i\frac{\beta_2(z)}{2}\omega^2 - i\epsilon_\Theta\right]\tilde{E}_m(z,\omega) + i\gamma(z)\tilde{E}_m(z,\omega)\star \\ \qquad \{\mathcal{F}[R(t')] \times \mathcal{F}[|E_m(z,t)|^2]\}. \end{cases}$$

All these noise sources are assumed proportional to the normal distribution. The standard derivations of $\epsilon_{\text{in}}$ and $\epsilon_\omega$ are determined by the laser's RIN PSD and frequency noise PSD, respectively.[53,54] To extend simulated Fourier frequency range to kHz frequencies, we examine this for a total of $2^{24}$ roundtrips.

### 2.3 Relative Intensity Noise and Self-Heterodyne Linear Interferometry

The filtered microcomb after removing the pump laser is measured by a photodetector (Thorlabs, Newton, New Jersey, United States, PDA10CF) with an optical power of 210 $\mu$W. A multimeter and an oscilloscope monitor the DC voltage ($V_0$). A signal source analyzer (Keysight, Santa Rosa, California, United States, E5052B) records the voltage fluctuation PSD $S_{\Delta I}(f)$. A home-built diffractive grating pair is used to select the comb lines for the timing jitter PSD measurement. We first optimize the noise floor of the self-heterodyne linear interferometer (SHLI) by improving the signal-to-noise ratio of the detected radio frequency (RF) signal at 100 MHz. Second, we minimize the relative delay time between the two optical comb lines ($\nu_n = 190.11$ THz, $\nu_m = 192.55$ THz) and the power difference of the two arms of SHLI to enable the suppression of the common-mode noise. Third, we optimize the delay time for the soliton microcomb based on two criteria: the first is to maximize the timing jitter measurement sensitivity, and the second is to expand the measured Fourier offset frequency range. The fiber delay length is optimized to be 49 m. The detected RF powers at the output of the two photodetectors are 14 and 19 dBm.

## 3 Results

### 3.1 Chip-Scale Low Timing Jitter Dispersion-Managed Silicon Nitride Microresonators

Figure 1(a) shows the schematic illustration of the DM soliton microcomb formation in the tapered microresonator, which includes scanning electron microscope images of the stoichiometric silicon nitride microresonator with an outer radius of 261 $\mu$m and a thickness of 800 nm. The nitride waveguide width is continuously changed from 1 to 4 $\mu$m to finely tune group velocity dispersion and filter high-order transverse modes in the single-mode microresonator.[52] GVD varies along the microresonator from $-55$ to 58 fs$^2$/mm simulated with the finite-element analysis method, as shown in Fig. 1(b) after considering both geometric and material dispersion. Figure 1(c) shows the simulated GVD for various waveguide widths along with the cavity path-averaged GVD calculated via the relation $\beta_2 = \int \beta_2(z)\mathrm{d}L/L_{\text{cavity}}$, where $\beta_2(z)$ is the GVD for the microresonator waveguide and $L_{\text{cavity}}$ is the cavity circumference.

The fundamental transverse-electric mode features a small anomalous path-averaged simulated GVD of $-3.51$ fs$^2$/mm at a pump wavelength of 1602 nm. The cavity GVD is experimentally characterized by swept-wavelength interferometry with only two AMX across the entire wavelength range for near single-mode operation. The measured free spectral range and GVD are ~89 GHz and $-4.39$ fs$^2$/mm, respectively, as shown in Fig. 1(d). These values deviate from the calculated dispersion due to factors such as fabrication imperfections, material inhomogeneity, and limitations in the accuracy of our measurement setup. The measured loaded and intrinsic quality factors are $1.8 \times 10^6$ and $3.4 \times 10^6$, respectively. Subsequently, we numerically examined the timing jitter PSD depending on different intrinsic cavity GVD, assuming no AMX, thermal, higher order dispersion, and Raman effects, as shown in Fig. 1(e). As the GVD decreases, the jitter PSD decreases. AMX will cause higher timing jitter PSD and higher integrated jitter accordingly, which will be proved in the numerical simulations, as shown in Fig. 1(f). These results show that the low-jitter pulse train can be realized by close-to-zero net dispersion and suppression of AMX. Our dispersion-managed adiabatic rings are able to suppress the occurrence of these avoided-mode crossings and obtain small dispersion, and thus reduce the timing jitter.

### 3.2 Thermally Stabilized Dispersion-Managed Microcomb Formation

DM microcombs are subsequently generated in the microresonator. Figure 2(a) illustrates the optical spectrum of the single-soliton DM microcomb overlapped with the numerically modeled spectral profile. Modest spectral dips resulting from two hybridized interpolarization-mode couplings at 1592.64 and 1659.72 nm are observed. The 1563.64 nm peak is the auxiliary pump laser. The effect of the auxiliary pump diminishes once the soliton state is reached. To maintain stability, thermal noise needs to be actively controlled through feedback mechanisms. To illustrate the temporal performance of the microcomb, we measured the intensity autocorrelation trace with a noncollinear second-harmonic autocorrelator after pump suppression with a bandpass filter. Figure 2(b) shows the measured pulse width of the single-soliton at ~305 fs for the filtered optical spectrum, along with the ~11.2 ps pulse train. The modeled pulse width is included in the inset of Fig. 2(d). We also observed double-soliton and soliton crystal states in the microresonator. The corresponding measured optical spectra of the double-soliton and one-defect soliton crystal are illustrated in Figs. 2(e) and 2(g) overlapped by the modeled spectral profiles, respectively. The soliton crystal optical spectrum indicates destructive interference between a single-soliton microcomb and a 12 free spectral range (FSR) perfect soliton crystal microcomb. The spatiotemporal modeled intracavity waveforms are depicted in Figs. 2(f) and 2(h), where the soliton defect in the time domain is presented. The demonstrated microcombs offer broader

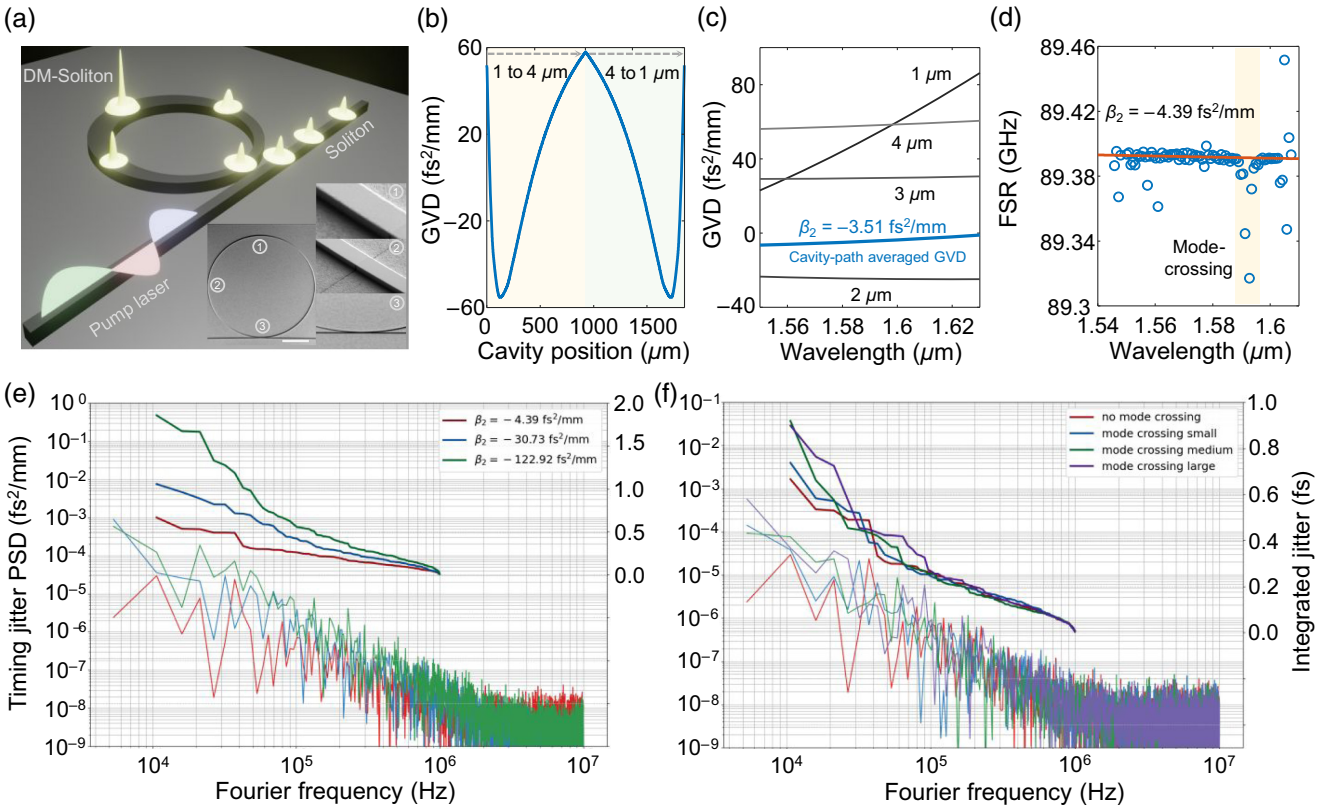


**Fig. 1** Chip-scale low timing jitter dispersion-managed silicon nitride microresonator. (a) Schematic illustration of DM soliton microcomb generation. Inset: scanning electron microscope images of the microresonator, zoomed waveguides, and the coupling gap. Scale bar: 130 $\mu$m. (b) Simulated GVD along the microresonator. (c) Simulated GVD of waveguides with different widths at a fixed waveguide height and the cavity path-averaged GVD. (d) Measured GVD via swept-wavelength interferometry showing $\beta_2 = -4.39$ fs$^2$/mm. (e) Modeled timing jitter PSD and integrated jitter versus Fourier frequency for a constant-dispersion uniform-width ring microcomb, with $\beta_2 = -4.39$, $-30.73$, and $-122.92$ fs$^2$/mm, respectively, no Raman and thermal effects assumed. (f) Modeled timing jitter PSD and integrated jitter versus Fourier frequency for a constant-dispersion uniform-width ring microcomb with different mode crossing levels.

optical spectra consistent with the simulated results over multiple soliton types with near single-mode operation with only two avoided-mode crossings and negligible center frequency shifts[55] compared with prior studies.[8–19]

### 3.3 Relative Intensity Noise Measurement of the Dispersion-Managed Microcombs

To obtain the DM microcombs reliably and deterministically, Fig. 3(a) illustrates the implemented TE–TM dual-driven pump approach (more details in the Supplementary Material, Sec. I). The forward-propagating pump laser is amplified and polarized into the transverse-electric (TE) polarization, whereas the backward-propagating transverse-magnetic (TM) polarized auxiliary laser thermally stabilizes the microresonator intracavity total power. Through this approach, we generate the microcombs in a planar tapered dispersion-managed $Si_3N_4$ microresonator at the effective red-detuned region of resonance $v_\mu$ based on dynamic photothermal stabilization. The orthogonally polarized auxiliary laser is blue-detuned from the resonant mode $v_{\mu+53}$ in the reverse direction to mitigate thermal transients during the microcomb transition from a high-noise chaotic state to a low-noise mode-locked state and stabilize the pump-resonance detuning thermally. The TM-polarized auxiliary laser experiences normal GVD and avoids the initiation of parametric oscillation while also stabilizing intracavity power via optimization of power and phase detuning.[43] To quantify the soliton microcomb noise performance, we conduct intensity noise at different soliton microcomb states prior to the respective timing jitter measurements. Coherence of the soliton frequency microcomb is examined via the RF intensity noise spectra over a microwave frequency span that is a few times the cold cavity resonance linewidth.

To supplement the RF intensity noise measurements of the soliton microcombs, measurement of the RIN is performed next. A signal source analyzer records the intensity fluctuation PSD of the soliton microcombs after suppressing the pump laser (detailed in Sec. 2). The filtered optical spectrum is shown in Fig. 3(b). The measured RIN PSD $[S_{\mathrm{RIN}}(f)]$ of the 89 GHz mode-locked microcombs, calculated by normalizing the measured intensity fluctuation PSD $[S_{\Delta V}(f)$ in units of V$^2$/Hz] by the average detected intensity $|V_0|^2$, is shown in Figs. 3(c)–3(e)

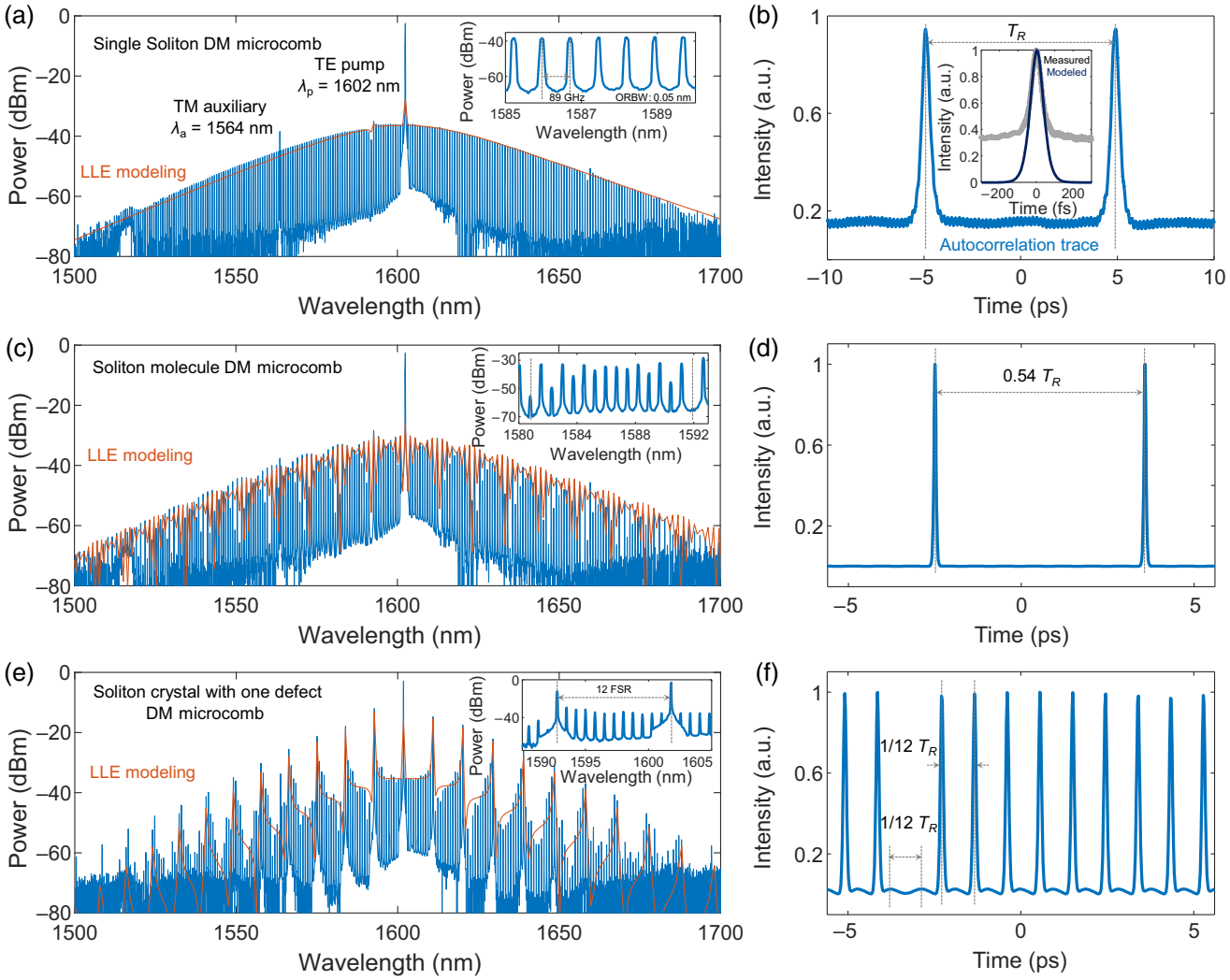


**Fig. 2** Soliton microcomb formation in tapered dispersion-managed microresonators. (a), (c), and (e) Measured optical spectra of the single-soliton, double-soliton, and one-defect soliton crystal DM microcombs overlapped with the numerical model, showing negligible center frequency shifts (detailed in the Supplementary Material). Insets are zoomed optical spectra. (b) Measured intensity autocorrelation trace of the single-soliton DM microcomb. Inset: measured and modeled pulse widths. (d) Modeled intracavity waveform of the double-soliton with a temporal separation of $0.54 \times T_R$. (f) Modeled intracavity waveform of the one-defect soliton crystal showing the modulated background (potential well) with a period of $1/12 \times T_R$.

corresponding to the single-soliton, double-soliton, and one-defect soliton crystal microcombs. The black curves in Figs. 3(c)–3(e) are the RIN PSD of the spatiotemporal chaotic state[53] (corresponding optical spectra are illustrated in the Supplementary Material, Sec. I, Fig. S1b2) and the pump laser, indicating the upper and lower bounds of the soliton microcomb RIN PSD. The soliton microcomb RIN PSD drops with a 30 dB/decade slope ($1/f^3$) over the first offset frequency decade, whereas the continuous-wave (CW) pump laser RIN PSD falls with a 20 dB/decade slope ($1/f^2$). The pump laser RIN PSD is measured at a nonresonant wavelength after the microresonator. The discrepancy between the two slopes is attributed to environmental noise sources such as free-space-to-chip coupling fluctuations. For the single-soliton state, the measured RIN is −153.2 dB/Hz at 100 kHz offset with a corresponding integrated RIN of 0.034% when integrated from 100 Hz to 10 MHz with the relation $\mathrm{RIN}_{\mathrm{in}} = \int_{f1}^{f2} S_{\mathrm{RIN}}(f)\mathrm{d}f$, where $f_1$ and $f_2$ are the lower and upper offset frequency bounds, respectively. The measured RIN of the double-soliton state and the soliton crystal state are −149.8 and −148.6 dB/Hz, respectively, for a 100 kHz offset. The corresponding integrated RINs are 0.036% and 0.023% over the same integrated frequency range. The inset of Fig. 3(c) shows the electrical noise suppression to facilitate the observation of the dynamical intensity noise of the microcombs by optimizing the incident power of the photodetector from −7.16 to −4.33 dBm. The insets of Figs. 3(d) and 3(e) show the noise degradation of the double-soliton and soliton crystal microcombs, which results from the conversion of phase fluctuations to intensity fluctuations in the intracavity spectral interference process.

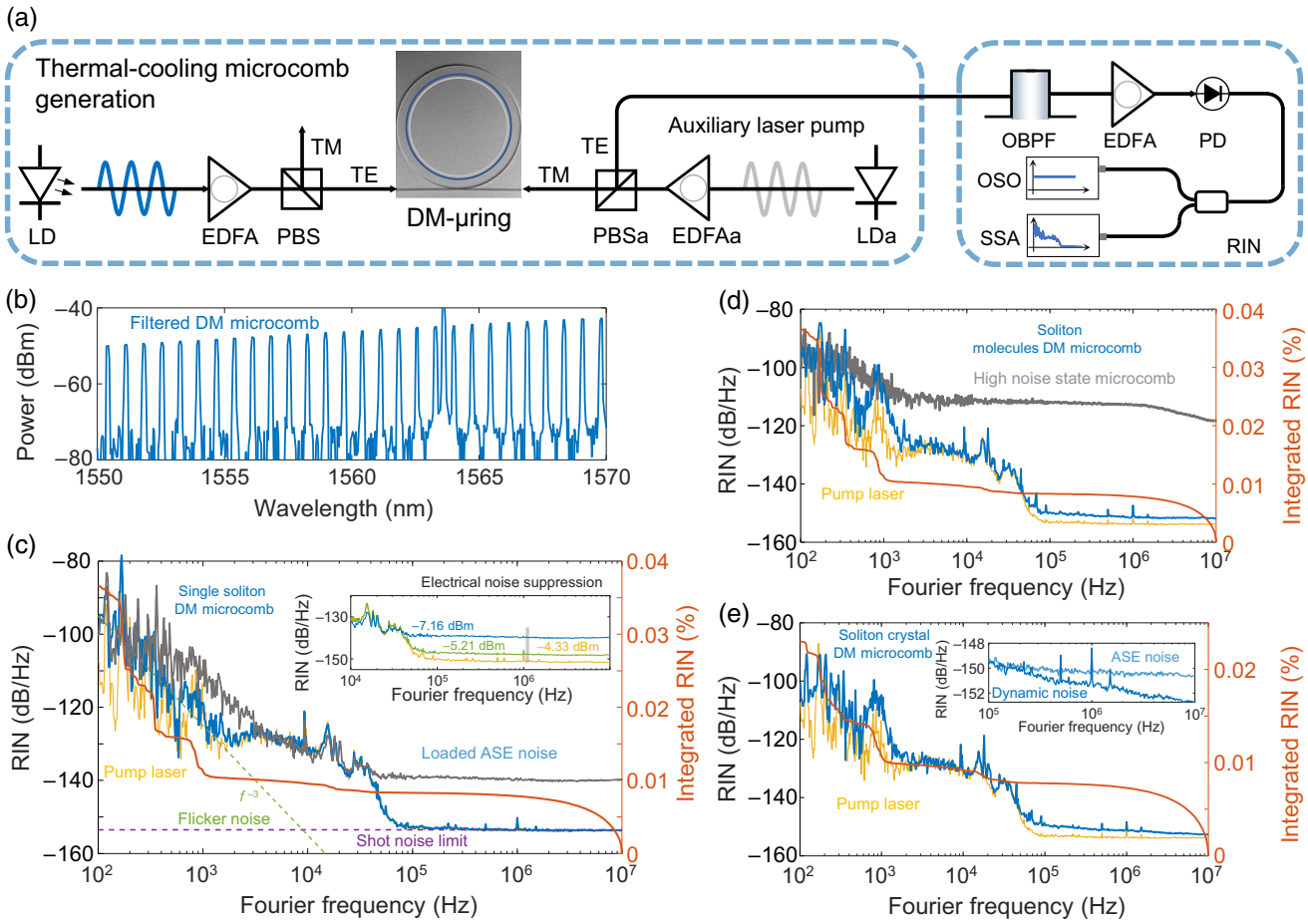


**Fig. 3** RIN measurements of the dispersion-managed microcombs. (a) Experimental setup of the TE–TM dual-driven approach for the generation of thermally stabilized soliton microcomb and the relative intensity noise measurement. LD, laser diode; EDFA, erbium-doped fiber amplifier; PBS, polarization beam splitter; TE, transverse-electric; TM, transverse-magnetic; OBPF, optical band-pass filter; PD, photodiode; OSO, oscilloscope; and SSA, signal source analyzer. (b) Filtered optical spectrum of the single-soliton DM microcomb. (c), (d), and (e) RIN PSD and the corresponding integrated RIN of the microcombs at different dynamical states along with the lower bound set by the pump laser. The RIN PSD of the chaotic DM microcomb and the RIN PSD after loading broadband amplified spontaneous emission (ASE) noise are also illustrated. Inset of (c): Electrical noise optimization by adjusting the incident optical power of the PD to explore the dynamic soliton intensity fluctuations at different states. Inset of (d): Noise degradation of the double-soliton DM microcomb showing additional white high-frequency noise. Inset of (e): Noise degradation of the soliton crystal DM microcomb showing dynamic high-frequency noise.

### *3.4 Self-Heterodyne Linear Interferometry for Soliton Microcomb Femtosecond Jitter Metrology*

We next examine the timing jitter via an SHLI. Figure 4(a) illustrates the implemented SHLI architecture for precision timing jitter metrology. The interferometer consists of a reference arm and a time-delayed arm in which a fiber-coupled acousto-optic modulator driven by an RF signal $f_m$ allows heterodyne detection of phase fluctuation power spectral density [PSD, $S_\varphi$ (dB rad$^2$/Hz)]. A diffractive-grating–based narrowband filter pair selects two microcomb lines at frequencies $\nu_n = n \times f_R + f_{\mathrm{CEO}}$ and $\nu_m = m \times f_R + f_{\mathrm{CEO}}$, as illustrated in the inset of Fig. 4(a) separated by a $(m-n) \times f_R$ frequency difference, where $f_R$ is the repetition rate and $f_{\mathrm{CEO}}$ is the carrier-envelope offset frequency of the microcombs. Frequency noise $\Delta\nu(f)$ of the selected lines is subsequently discriminated with the delay time $\tau$ by the relation $\Delta\phi(f) = 2\pi\Delta\nu(f)\tau$. The optical phase fluctuations $\Delta\phi(f)$ are converted into optical intensity fluctuations by linear optical interferometry. At the fiber interferometer output, the two optical lines are demodulated by two photodetectors. The residual phase noise PSD originates from the frequency difference $(m-n) \times f_R$ of the two selected comb lines, proportional to the delay time $\tau$. Then, a double-balanced mixer is used to extract the timing jitter PSD and eliminate the common-mode noise induced by the carrier-envelope offset signal and the driven microwave frequency signal ($f_m$). The frequency fluctuations of the two selected optical comb lines are converted into voltage fluctuations with the transfer function $\Delta V(f) \propto K_\varphi \frac{|1-e^{-i2\pi f\tau}|}{|i\times f|}(m-n)\Delta f_R(f)$, where $K_\varphi$ is the peak

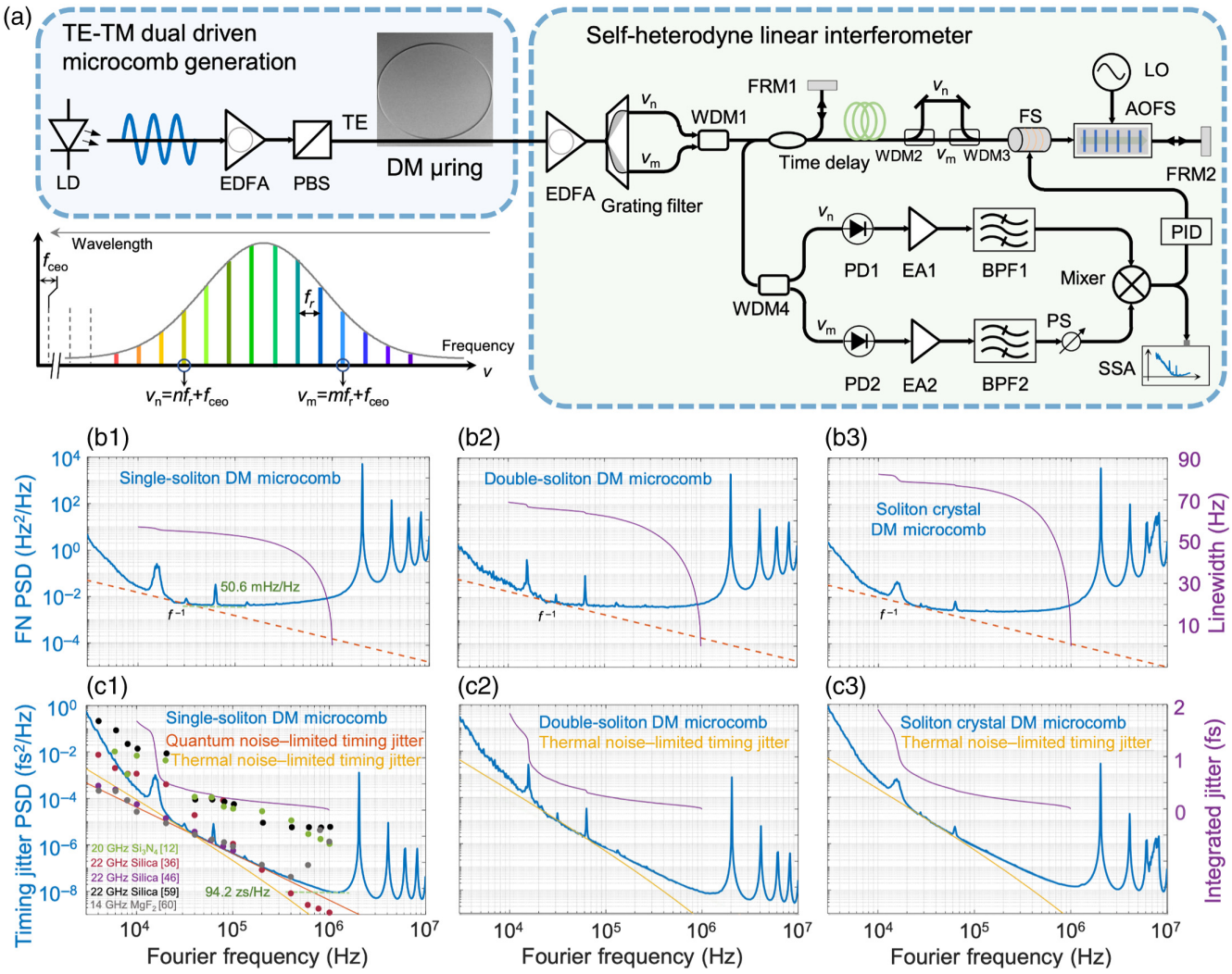


**Fig. 4** Measured repetition-rate frequency noise PSD and timing jitter PSD and the corresponding integrated RF linewidth and timing jitter of dispersion-managed soliton microcombs. (a) Experimental setup of the SHLI. WDM, wavelength division multiplexer; FS, fiber stretcher; EA, electronic amplifier; BPF, bandpass filter; PS, phase shifter; PID, proportional–integral–differential controller. Inset: schematic illustration of the SHLI. (b1), (b2), and (b3) Measured frequency noise PSD at different soliton states with a 49 m stabilized fiber link. The orange dashed lines with 10 dB/decade slopes indicate repetition-rate frequency free-walk induced by microresonator intracavity power fluctuations. The corresponding repetition-rate tone linewidth integrated from 1 MHz to 10 kHz is denoted with purple curves. The repetition-rate carrier frequency is 89 GHz. (c1), (c2), and (c3) Timing jitter PSD measurement of the soliton microcombs at different dynamical states with the calculated thermal-noise and quantum-noise limits. The timing jitter theoretical models from Refs. 56 and 57 are quantum-noise and thermal-noise limits of the soliton microcombs denoted, respectively, with solid orange and yellow lines. The corresponding integrated timing jitter is included. The comparison between the measured timing jitter PSD and prior works[12,34,44,58,59] is included as well.

voltage at the double-balanced mixer output. The transfer function shows that the measured voltage fluctuation is proportional to $|1-e^{-i2\pi f\tau}|/|i\times f|$, which implies there will be null points at the offset frequency $f=1/\tau$ and its harmonics, providing the upper Fourier frequency limit of the timing jitter measurement.

The measured voltage fluctuation PSD is subsequently converted into frequency noise PSD and further into timing jitter PSD $S_{\Delta T_R}(f)$ with the relation $S_{\Delta T_R}(f)=(\frac{1}{2\pi f_R})^2\frac{1}{(m-n)^2}\frac{1}{f^2}(\frac{|i\times f|}{K_\varphi|1-e^{-i2\pi f\tau}|})^2 S_{\Delta V}(f)$. The detected voltage fluctuation at the mixer output is separated into two parts. The first part synchronizes the fiber interferometer to the frequency microcombs, avoiding free walk via a piezoelectric-transduced fiber stretcher (FS) through a loop filter with 1 kHz bandwidth. The second part is recorded by a signal source analyzer, which gives the timing fluctuation PSD and the frequency fluctuation PSD of the soliton microcomb repetition rate. To precisely remove

the common-mode noise resulting from dispersion and increase the interferometer signal-to-noise ratio, we utilize a delay control unit, which contains a motorized fiber delay line and a pair of wavelength division multiplexing (WDM) couplers. This timing-stabilized and dispersion-compensated fiber interferometer can be considered a true time delay, which is an optical counterpart of the delay line frequency discriminator in microwave metrology.[60]

We convert the measured voltage fluctuation PSD on the baseband into the repetition-rate frequency noise $S_{\Delta f_R}$ PSD to examine the frequency noise behavior, as shown in Figs. 4(b1)–4(b3) of the soliton microcomb at the single-soliton, double-soliton, and soliton crystal states, respectively. The measured repetition-rate frequency noise PSD are 2556, 4151, and 4168 $\mathrm{mHz}^2/\mathrm{Hz}$, respectively, at 100 kHz offset with a noise frequency resolution of 64 $\mathrm{mHz}/\mathrm{Hz}^{1/2}$ at the single-soliton microcomb. We observe that the repetition-rate frequency noise features a 20 dB/decade slope below ~20 kHz offset, indicating the repetition-rate random walk frequency noise. Based on the power-law noise, soliton microcombs have a repetition-rate flicker frequency walk from ~20 to 40 kHz offset, a white frequency noise from ~40 to 200 kHz offset, and a flicker and white phase noise from ~200 kHz to 1 MHz. The resulting integrated linewidths of the free-running repetition-rate tone are shown in Fig. 4(b) for the three microcomb dynamical states. We also note that the repetition-rate close-to-carrier phase noise can be stabilized to a low-noise microwave oscillator.[24]

Figures 4(c1)–4(c3) show the measured timing jitter PSD for different soliton dynamical states. For the single-soliton comb, the measured quantum-noise–limited timing jitter PSD is 0.4 $\mathrm{as}^2/\mathrm{Hz}$ at 100 kHz offset. The corresponding integrated timing jitter is 1.7 fs ± 0.07 fs when integrated from 10 kHz to 1 MHz, as shown in Fig. 4(c1), which is close to the timing jitter in silica microresonator frequency microcombs measured with similar technology.[34] The integrated timing jitter from 10 kHz to 44.5 GHz Nyquist is ~32.3 fs. The achieved femtosecond-level jitter is enabled by close-to-zero intracavity dispersion to minimize group delay fluctuations, suppressed Kerr nonlinearities within the tapered waveguide,[45] and the thermally stabilized dual-driven approach. Our dispersion-managed microresonator stretches the soliton pulse within the cavity, reducing the accumulated nonlinear phase shift during pulse propagation. The quantum-noise–limited timing jitter PSD of the two (double-soliton and soliton crystal) states at 100 kHz offset are at 0.66 and 0.82 $\mathrm{as}^2/\mathrm{Hz}$, respectively. This corresponds to an integrated jitter of 1.9 fs ± 0.06 fs and 1.8 fs ± 0.09 fs. The dynamical noise is observed in the timing jitter PSD of the soliton crystal microcomb at the offset frequency of ~8 MHz. Compared with direct photon detection for timing jitter PSD measurements,[12] the SHLI method can effectively avoid the IM-PM conversion and shot-noise limit. The measured timing jitter PSD is comparable to prior works,[12,34,44,57,58] as shown in Fig. 4(c1).

For each of the microcomb soliton states, we observe that the timing jitter PSD drops with a 40 dB/decade slope within 3 to 20 kHz, as shown in Fig. 4(c). Deviation of timing jitter PSD over low Fourier frequency is associated with intracavity power fluctuation leading to a $1/f^4$ slope with the relation $S_{\Delta T_R}^{T_R}(f) = (\frac{1}{2\pi f T_R})^2 S_{T_R}(f)$ where intracavity power-induced roundtrip fluctuations $S_{T_R} \propto f^{-2}$.

Figure 4(c) also plots the theoretical cavity thermal bounds on the timing jitter PSD with the yellow solid line, arising from thermo-refractive variation and bounding the measured timing jitter PSD from 20 to 40 kHz with a 25 dB/decade slope ($1/f^{2.5}$). In the DM microresonator, the thermal-noise–limited timing jitter PSD, originating from the thermodynamic fluctuations $\langle \delta T^2 \rangle = k_B T^2/\mathrm{CV}\rho$, where $V$ is the optical mode volume, $k_B$ is the Boltzmann constant, $T$ is the chip temperature, $\rho$ is the density, and $C$ is the specific heat capacity, is described with the following model:[61]

$$S_{\Delta T_R}(f) = \frac{1}{(2\pi f_R)^2}\left(\frac{v_c}{f_R}\frac{1}{n_0}\frac{dn}{dT}\right)^2 \frac{1}{f^2}\frac{k_B T^2}{\sqrt{2\pi^4 \kappa \rho C f}} \times \frac{1}{R\sqrt{d_r^2 - d_z^2}}\frac{1}{[1+(2\pi f \tau_d)^{3/4}]^2}, \tag{1}$$

where $dn/dT$ is the thermorefractive coefficient, $\kappa$ is the thermal conductivity, $R$ is the microresonator ring radius, $d_{r(z)} = \int \mathrm{d}_{r(z)} \mathrm{d}L/L_{\mathrm{cavity}}$ is the half-width of the fundamental mode along the tapered DM microresonator, and $\tau_d = \frac{\pi^{1/3}}{4^{1/3}}\frac{\rho C}{\kappa} d_r^2$. From 40 to 600 kHz, the measured PSD falls with a quantum-noise–limited 20 dB/decade slope ($1/f^2$). The theoretical quantum-noise timing jitter limit without shot noise is shown in Fig. 4(c) with the orange solid lines following the model[56]

$$S_{\Delta T_R}(f) = \frac{1}{4\pi\sqrt{2} f_R^2}\sqrt{\frac{\gamma}{\Delta_0 D}}\frac{g}{\gamma^2}\left[\frac{1}{96}\frac{\gamma D}{\Delta_0}\frac{\gamma^2}{f^2} + \frac{1}{24}\left(1+\frac{\pi^2 f^2}{\gamma^2}\right)^{-1}\frac{\gamma^2}{f^2}\frac{\Delta_0 D}{\gamma}\right], \tag{2}$$

where $\gamma$ is the half linewidth half height of the cavity resonance, $f_R$ is the repetition rate of the microcombs, $g = \frac{n_2}{n_0}\frac{\hbar\omega_c^2 c}{V n_0}$ is the nonlinear gain coefficient, $n_0(n_2)$ is the refractive index (nonlinear index) of the nitride resonator, $\omega_c = 2\pi v_c$, $v_c$ is the center frequency of the microcombs, $c$ is the light speed in vacuum, $D = -\frac{\beta_2 \omega_R^2 c}{\gamma n_0}$ is the normalized dispersion, and $\Delta_0 = \omega_0 - \omega_P$ is the resonance-pump detuning. Above 600 kHz, the measured PSD is limited to 8905 $\mathrm{zs}^2/\mathrm{Hz}$ by the SHLI spectral resolution.

Based on soliton theory, the quantum-noise–limited timing jitter PSD model, especially in the high offset frequency more than 10 kHz, can analytically predict noise behaviors for different mode-locked states via the relation $\mathrm{S}_{\Delta T_R}(f) \approx 0.5294 \frac{\xi}{(2\pi f)^2}\frac{h\nu}{E_p}\frac{\alpha_{\mathrm{tot}}}{T_R}\tau_p^2$,[57] where $E_p \approx \frac{4\pi h \theta v_c}{D_1 \gamma_c}\sqrt{2 D_2 \Delta_0}$ is the intracavity pulse energy, $D_1/2\pi$ is the cavity FSR, $D_2$ is related to the cavity GVD, $\theta$ is the transmission of the microresonator, $\gamma_c$ is the cubic nonlinearity parameter, $\tau_p \approx \frac{1}{D_1}\sqrt{\frac{D_2}{2\Delta_0}}$ is the intracavity pulse duration,[37] $\xi$ and $\alpha_{\mathrm{tot}}$ are the spontaneous emission factor and cavity loss, respectively. For different soliton states, the quantum-noise–limited timing jitter PSD is inversely proportional to the resonance-pump detuning and proportional to square root of the cavity dispersion. The soliton microcomb center frequency fluctuation PSD $\mathrm{S}_{\Delta v_c}(f)$ can also be converted into the timing jitter with the relation $\mathrm{S}_{\Delta T_R}(f) \approx (\frac{D_2}{f T_R})^2 \mathrm{S}_{\Delta v_c}(f)$, where $\Delta v_c$ is the center frequency fluctuations induced by avoided-mode crossings,[39,40] odd-order dispersion,[42] or Raman effects.[55] In addition, the intracavity intensity fluctuations will introduce the extra timing jitter PSD with the relation of

$S_{\Delta T_R}(f) = C \times (\eta P_{\text{in}})^2 (\frac{1}{f})^2 S_{\text{RIN}}(f)$, where $\eta = df_R/dP_{\text{in}}$ is the transduction factor, $P_{\text{in}}$ is the microresonator intracavity power, and $C$ is a constant.[34,43]

We note our noise measurements of the frequency microcombs below the offset frequency of 20 kHz are still higher than the microresonator theoretical thermodynamical limits. This is attributed to the strong free-running intracavity power fluctuations and pump-resonance detuning noise. Further active stabilization of the intracavity power and pump-resonance detuning[33,40] can improve the timing jitter PSD at the low-offset frequency. By increasing the tapered waveguide width (increasing the effective resonant mode volume) and decreasing the cavity GVD, the jitter of the frequency DM microcomb oscillator can be improved to subfemtosecond timing imprecision.

## 4 Conclusion

In this study, the fundamental noise of dispersion-managed soliton microcombs without a restoring force is examined in detail. Dispersion-managed microcombs are deterministically and reliably generated with a TE–TM dual-driven thermally stabilized approach at the single-soliton, double-soliton, and soliton crystal regimes. The RIN is determined to be $-153.2$ dB/Hz at 100 kHz offset for the single-soliton state, with parameters bounded by the CW pump laser. The timing jitter PSD is 0.4 as$^2$/Hz at 100 kHz offset, and the corresponding integrated timing jitter is 1.7 fs $\pm$ 0.07 fs from 10 kHz to 1 MHz ($\approx$32.3 fs from 10 kHz to Nyquist 44.5 GHz). To the best of our knowledge, we achieved femtosecond timing jitter for the first time in dispersion-managed microcombs. The demonstrated results show that the dynamic noise for the double-soliton and soliton crystal in the RIN PSD is important to understand intracavity soliton dynamics, with the single-soliton state having the lowest jitter and with slight but quantifiable variations across different soliton states.

The primary noise source at low-offset frequencies is the fluctuation in effective cavity length, which arises from intracavity power fluctuations in the microresonator. In dispersion-managed microcombs, we observe negligible center frequency shifts, which helps to prevent noise conversion processes related to center frequency shifts. Future studies could explore how high-order dispersion in these microresonators facilitates additional noise coupling mechanisms. By implementing feedback to stabilize the pump laser's intracavity power and frequency, the timing jitter of the dispersion-managed chip-scale soliton oscillator could be reduced to subfemtosecond levels. Furthermore, balancing factors such as detuning, nonlinearity, higher order dispersion, and avoided-mode crossing in the microresonator can further minimize timing jitter.

## Disclosures

The authors declare that there are no financial interests, commercial affiliations, or other potential conflicts of interest that could have influenced the objectivity of this research or the writing of this paper.

## Code and Data Availability

Availability of code, data, and/or materials used in the research results reported in this paper may be provided upon reasonable request.

## Author Contributions

W. W. and H. L. conducted the experiments. W. W. and W. L. analyzed the data. W. W., H. L., and W. L. contributed to the simulations. W. L. performed the noise simulations. J. Y. designed the microresonator. T. M., D. L., J. Y., A. K. V., J. L., and Y. S. J. contributed to the design of the experiments. M. Y. and D.-L. K. performed the device nanofabrication. W. W., J. Y., P. D., J. C., and C. W. W. initiated the project. W. W. and C. W. W. wrote the paper. All authors discussed the results. Correspondence and requests for materials should be addressed to W. L. and C. W. W. (wzliu@g.ucla.edu; cheewei.wong@ucla.edu).

### Acknowledgments

The authors acknowledge fruitful discussions with Shu-Wei Huang, Scott Diddams, Tara Drake, and Dohyeon Kwon on the measurements, with Guo Qing Chang and Ming Xin on noise theory, and with Ken Yang. We acknowledge financial support from the Lawrence Livermore National Laboratory (Grant No. B622827), the National Science Foundation (Grant Nos. 1824568, 1810506, 1741707, and 1829071), and the Office of Naval Research (Grant No. N00014-16-1-2094).

### References

1. S. A. Diddams, K. Vahala, and T. Udem, "Optical frequency combs: coherently uniting the electromagnetic spectrum," *Science* **369**, 267 (2020).
2. A. L. Gaeta, M. Lipson, and T. J. Kippenberg, "Photonic-chip-based frequency combs," *Nat. Photonics* **13**, 158–169 (2019).
3. M. Lezius et al., "Space-borne frequency comb metrology," *Optica* **3**, 1381–1386 (2016).
4. J. Lee et al., "Testing of a femtosecond pulse laser in outer space," *Sci. Rep.* **4**, 5134–5137 (2014).
5. I. Coddington et al., "Rapid and precise absolute distance measurements at long range," *Nat. Photonics* **3**, 351–356 (2009).
6. I. Kudelin et al., "Photonic chip-based low-noise microwave oscillator," *Nature* **627**, 534–539 (2024).
7. W. T. Wang et al., "Coherent terahertz radiation with 2.8-octave tunability through chip-scale photomixed microresonator optical parametric oscillation," *Nat. Commun.* **13**, 5123 (2022).
8. T. J. Kippenberg et al., "Dissipative Kerr solitons in optical microresonators," *Science* **361**, 8083 (2018).
9. T. Herr et al., "Temporal solitons in optical microresonators," *Nat. Photonics* **8**, 145–152 (2014).
10. A. Tikan et al., "Emergent nonlinear phenomena in a driven dissipative photonic dimer," *Nat. Phys.* **17**, 604–610 (2021).
11. V. Brasch et al., "Photonic chip–based optical frequency comb using soliton Cherenkov radiation," *Science* **351**, 357–360 (2016).
12. Q. Liu et al., "Photonic microwave generation in the X- and K-band using integrated soliton microcombs," *Nat. Photonics* **14**, 486–491 (2020).
13. X. W. Liu et al., "Aluminum nitride nanophotonics for beyond-octave soliton microcomb generation and self-referencing," *Nat. Commun.* **12**, 5428 (2021).
14. Y. He et al., "High-speed tunable microwave-rate soliton microcomb," *Nat. Commun.* **14**, 3467 (2023).
15. L. Chang et al., "Ultra-efficient frequency comb generation in AlGaAs-on-insulator microresonators," *Nat. Commun.* **9**, 1869 (2018).
16. M. H. Zhang et al., "Strong interactions between solitons and background light in Brillouin-Kerr microcombs," *Nat. Commun.* **15**, 1661 (2024).

17. A. S. Raja et al., "Electrically pumped photonic integrated soliton microcomb," *Nat. Commun.* **10**, 680 (2019); correction **10**, 1623 (2019).
18. B. Q. Shen et al., "Integrated turnkey soliton microcombs," *Nature* **582**, 365–369 (2020).
19. W. Jin et al., "Hertz-linewidth semiconductor lasers using CMOS-ready ultrahigh-Q microresonators," *Nat. Photonics* **15**, 346–353 (2021).
20. P. Marin-Palomo et al., "Microresonator-based solitons for massively parallel coherent optical communications," *Nature* **546**, 274–279 (2017).
21. A. Fülöp et al., "High-order coherent communications using mode-locked dark-pulse Kerr combs from microresonators," *Nat. Commun.* **9**, 1598 (2018).
22. B. Corcoran et al., "Ultra-dense optical data transmission over standard fibre with a single chip source," *Nat. Commun.* **11**, 2568 (2020).
23. J. Riemensberger et al., "Massively parallel coherent laser ranging using a soliton microcomb," *Nature* **581**, 164–170 (2020).
24. E. Obrzud et al., "A microphotonic astrocomb," *Nat. Photonics* **13**, 31–35 (2019).
25. G. Suh et al., "Searching for exoplanets using a microresonator astrocomb," *Nat. Photonics* **13**, 25–30 (2019).
26. G. Suh et al., "Microresonator soliton dual-comb spectroscopy," *Science* **354**, 600–603 (2016).
27. A. Dutt et al., "On-chip dual-comb source for spectroscopy," *Sci. Adv.* **4**, e1701858 (2018).
28. M. J. Yu et al., "Silicon-chip-based mid-infrared dual-comb spectroscopy," *Nat. Commun.* **9**, 1869 (2018).
29. Y.-S. Jang et al., "Nanometric precision distance metrology via hybrid spectrally-resolved and homodyne interferometry in a single-soliton frequency microcomb," *Phys. Rev. Lett.* **126**, 023903 (2021).
30. M. G. Suh and K. J. Vahala, "Soliton microcomb range measurement," *Science* **359**, 884–887 (2018).
31. P. Trocha et al., "Ultrafast optical ranging using microresonator soliton frequency combs," *Science* **359**, 887–891 (2018).
32. C. H. Lao et al., "Quantum decoherence of dark pulses in optical microresonators," *Nat. Commun.* **14**, 1802 (2023).
33. E. Lucas et al., "Ultralow-noise photonic microwave synthesis using a soliton microcomb-based transfer oscillator," *Nat. Commun.* **11**, 374 (2020).
34. J. Feldmann et al., "Parallel convolutional processing using an integrated photonic tensor core," *Nature* **589**, 52–58 (2021).
35. D. Jeong et al., "Ultralow jitter silica microcomb," *Optica* **7**, 1108 (2020).
36. X. Y. Xu et al., "11 TOPS photonic convolutional accelerator for optical neural networks," *Nature* **589**, 44–51 (2021).
37. E. Lucas et al., "Detuning-dependent properties and dispersion-induced instabilities of temporal dissipative Kerr solitons in optical microresonators," *Phys. Rev. A* **95**, 043822 (2017).
38. J. R. Stone et al., "Thermal and nonlinear dissipative-soliton dynamics in Kerr-microresonator frequency combs," *Phys. Rev. Lett.* **121**, 063902 (2018).
39. A. Aldhafeeri et al., "Low phase noise K-band signal generation using polarization diverse single-soliton integrated microcombs," *Photonics Res.* **12**, 1175–1185 (2024).
40. Q.-F. Yang et al., "Dispersive-wave induced noise limits in miniature soliton microwave sources," *Nat. Commun.* **12**, 1442 (2021).
41. Y. Bai et al., "Brillouin-Kerr soliton frequency combs in an optical microresonator," *Phys. Rev. Lett.* **126**, 063901 (2021).
42. J. R. Stone and S. B. Papp, "Harnessing dispersion in soliton microcombs to mitigate thermal noise," *Phys. Rev. Lett.* **125**, 153901 (2020).
43. T. E. Drake et al., "Thermal decoherence and laser cooling of Kerr microresonator solitons," *Nat. Photonics* **14**, 480–485 (2020).
44. C. Bao et al., "Quantum diffusion of microcavity solitons," *Nat. Phys.* **17**, 462–466 (2021).
45. Y. Li et al., "Real-time transition dynamics and stability of chip-scale dispersion-managed frequency microcombs," *Light Sci. Appl.* **9**, 52 (2020).
46. C. Bao and C. Yang, "Stretched cavity soliton in dispersion-managed Kerr resonators," *Phys. Rev. A* **92**, 023802 (2015).
47. J. Taylor et al., "Characterization of power-to-phase conversion in high-speed P-I-N photodiodes," *IEEE Photo. J.* **3**, 140–151 (2011).
48. D. Kwon et al., "Reference-free, high-resolution measurement method of timing jitter spectra of optical frequency combs," *Sci. Rep.* **7**, 40917 (2017).
49. A. Kordts et al., "Higher order mode suppression in high-Q anomalous dispersion SiN microresonators for temporal dissipative Kerr soliton formation," *Opt. Lett.* **41**, 452–455 (2016).
50. M. H. Anderson et al., "Dissipative solitons and switching waves in dispersion-modulated Kerr cavities," *Phys. Rev. X* **13**, 011040 (2023).
51. W. T. Wang et al., "Polarization-diverse soliton transitions and deterministic switching dynamics in strongly-coupled and self-stabilized microresonator frequency combs," *Comm. Phys.* **7**, 279 (2024).
52. M. Karpov et al., "Dynamics of soliton crystals in optical microresonators," *Nat. Phys.* **15**, 1071–1077 (2019).
53. C. Godey et al., "Stability analysis of the spatiotemporal Lugiato-Lefever model for Kerr optical frequency combs in the anomalous and normal dispersion regimes," *Phys. Rev. A* **89**, 063814 (2014).
54. F. Lei et al., "Optical linewidth of soliton microcombs," *Nat. Commun.* **13**, 3161 (2022).
55. L. Hu et al., "Theory of soliton self-frequency shift in silica optical microresonators with a modified Raman response by the Boson peak," *Opt. Express* **32**, 4062–4071 (2024).
56. A. B. Matsko and L. Maleki, "On timing jitter of mode-locked Kerr frequency combs," *Opt. Express* **21**, 28862–28876 (2013).
57. R. Paschotta, "Noise of mode-locked lasers (Part II): timing jitter and other fluctuations," *Appl. Phys. B* **79**, 163–173 (2004).
58. X. Yi et al., "Soliton frequency comb at microwave rates in a high-Q silica microresonator," *Optica* **2**, 1078–1085 (2015).
59. W. Weng et al., "Spectral purification of microwave signals with disciplined dissipative Kerr solitons," *Phys. Rev. Lett.* **122**, 013902 (2019).
60. S. H. Huang et al., "Precise measurement of ultra-narrow laser linewidths using the strong coherent envelope," *Sci. Rep.* **7**, 41988 (2016).
61. G. Huang et al., "Thermorefractive noise in silicon-nitride microresonators," *Phys. Rev. A* **99**, 061801 (2019).
62. S. W. Huang et al., "Smooth and flat phase-locked Kerr frequency comb generation by higher order mode suppression," *Sci. Rep.* **6**, 26255 (2016).
63. D. Owen, "Good practice guide to phase noise measurement," Measurement Good Practice Guide 68 (2004).
64. E. Rubiola et al., "Photonic-delay technique for phase-noise measurement of microwave oscillators," *J. Opt. Soc. Am. B* **22**, 987 (2005).
65. D. Hou et al., "Timing jitter characterization of mode-locked lasers with <1zs/Hz resolution using a simple optical heterodyne," *Opt. Lett.* **40**, 2985–2988 (2015).
66. C. Kim et al., "Sub-femtosecond timing jitter, all-fiber, CNT-mode-locked Er-laser at telecom wavelength," *Opt. Express* **21**, 26533–26541 (2013).
67. Y. Song, K. Jung, and J. Kim, "Impact of pulse dynamics on timing jitter in mode-locked fiber lasers," *Opt. Lett.* **36**, 1761–1763 (2011).
68. B. Razavi, "Jitter-power trade-offs in PLLs," *IEEE Trans. Circuits Syst.* **68**, 1381–1387 (2021).
69. A. Morton and M. J. Morton, "High-power, ultra-low noise hybrid lasers for microwave photonics and optical sensing," *J. Light. Technol.* **36**, 5048–5057 (2018).
70. D. C. Heinecke, A. Bartels, and S. A. Diddams, "Offset frequency dynamics and phase noise properties of a self-referenced 10 GHz

Ti:sapphire frequency comb," *Opt. Express* **19**, 18440–18451 (2011).
71. A. Klenner et al., "Gigahertz frequency comb from a diode-pumped solid-state laser," *Opt. Express* **22**, 31008–31019 (2014).
72. J. Chen et al., "High repetition rate, low jitter, low intensity noise, fundamentally mode-locked 167 fs soliton Er-fiber laser," *Opt. Lett.* **32**, 1566–1568 (2007).

**Wenting Wang** received his PhD from the Institute of Semiconductors, Chinese Academy of Sciences, Beijing, China, and Deutsches Elektronen-Synchrotron, Hamburg, Germany, in 2017. From 2017 to 2022, he was a postdoctoral fellow at the University of California, Los Angeles. He is currently a professor at the Xiongan Institute of Innovation, Chinese Academy of Sciences, Xiongan, China. His research interests include ultralow-noise microwave/terahertz generation, micro-cavity optical frequency combs, optical signal processing, integrated microwave photonics, and high-precision time and frequency transfer.

**Wenzheng Liu** is a PhD student in the Department of Electrical Engineering at the University of California, Los Angeles. He received his BS degree from the University of Science and Technology of China in 2018 and then received his MS degree from the California Institute of Technology in 2020. His research interests include micro-cavity optical frequency combs, integrated microwave photonics, quantum optics, and computer vision.

**Ninghua Zhu** received the BS, MS, and PhD degrees in electronic engineering from the University of Electronic Science and Technology of China, Chengdu, China, in 1982, 1986, and 1990, respectively. From 1990 to 1994, he was a postdoctoral fellow at Sun Yat-sen University, Guangzhou, China, where he became an associate professor in 1992 and a full professor in 1994. He is currently a professor at the Institute of Semiconductors, Chinese Academy of Sciences, Beijing, China. He has authored or co-authored more than 200 journal papers, three books, and three book chapters. He is an associate editor for *Optics Express*. His research interests include modeling and characterization of integrated optical waveguides and coplanar transmission lines and optimal design of optoelectronics devices and photonic integrated circuits.

**Chee Wei Wong** received his BS degree in mechanical engineering from the University of California at Berkeley, in 1999, and his MS and PhD degrees from the Massachusetts Institute of Technology (MIT), Cambridge, in 2001 and 2003, respectively. He was a postdoctoral fellow at the MIT in 2003. He is currently a professor at the Electrical Engineering Department of the University of California, Los Angeles. He is a fellow of the American Physical Society. His current research interests include nonlinear and quantum optics in nanophotonics, silicon electronic–photonic circuits and photonic crystals, quantum dot interactions in nanocavities, nano-electromechanical systems, and nanofabrication.

Biographies of the other authors are not available.

**Supplementary Information**

# Mapping ultrafast timing jitter in dispersion-managed 89 GHz frequency microcombs via self-heterodyne linear interferometry

**Wenting Wang[1,2,†], Wenzheng Liu[1,*,†], Hao Liu[1,†], Tristan Melton[1], Alwaleed Aldhafeeri[1], Dong-IL Lee[1], Jinghui Yang[1], Abhinav Kumar Vinod[1], Jinkang Lim[1], Yoon-Soo Jang[1], Heng Zhou[3], Mingbin Yu[4,5], Patrick Guo-Qiang Lo[4,6], Dim-Lee Kwong[4], Peter DeVore[7], Jason Chou[7], Ninghua Zhu[8] and Chee Wei Wong[1,*]**

[1] Fang Lu Mesoscopic Optics and Quantum Electronics Laboratory, University of California, Los Angeles, CA 90095, United States of America

[2] Mesoscopic Optics and Advanced Instruments Laboratory, School of Optics and Photonics, Beijing Institute of Technology, Beijing, China

[3] Key Lab of Optical Fiber Sensing and Communication Networks, University of Electronic Science and Technology of China, Chengdu 611731, China

[4] Institute of Microelectronics, A*STAR, Singapore 117865, Singapore

[5] State Key Laboratory of Functional Materials for Informatics, Shanghai Institute of Microsystem and Information Technology, and Shanghai Industrial Technology Research Institute, Shanghai, China

[6] Advanced Micro Foundry, Singapore 117685, Singapore

[7] Lawrence Livermore National Laboratory, Livermore, CA 94550, United States of America

[8] Institute of Intelligent Photonics, Nan Kai University, Tianjin, China

[†] These authors contributed equally to this work.

[*] To whom correspondence should be addressed. Email: wzliu@g.ucla.edu; cheewei.wong@ucla,edu

## Supplementary Information Content



## I. Measurements of microcomb center frequency shift, timing jitter and pump intensity noise

The single-soliton microcomb center frequency shifts are measured in the dispersion-managed [62] and uniform microresonators, as shown in Figures S1a and S1b, respectively. In the dispersion-managed microresonator, the center frequency shift of the microcomb is negligible in

contrast with a 4.65 nm wavelength shift of a 2 μm waveguide width uniform microresonator when pumping at the similar wavelength.

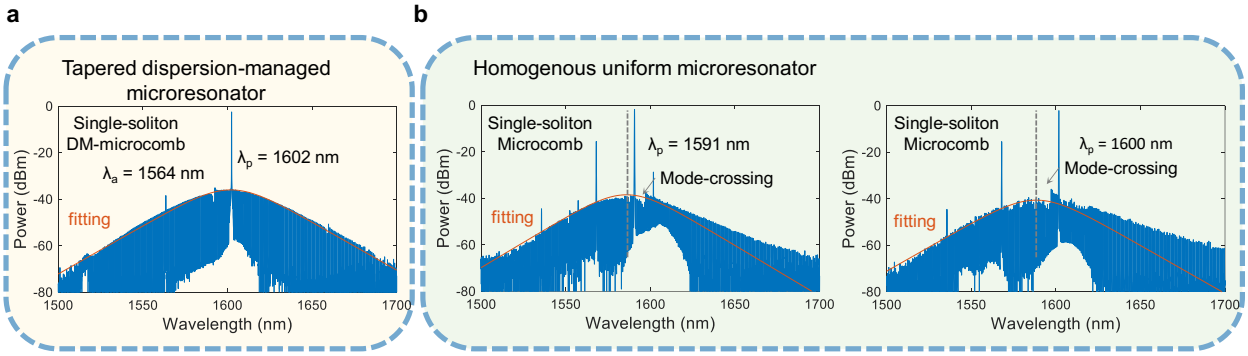


**Figure S1 | Single-soliton optical spectra generated in the dispersion-managed and homogenous uniform microresonators. a,** Single-soliton optical spectrum from a dispersion-managed microresonator. **b,** Single-soliton optical spectra generated in a uniform microresonator at different pump wavelengths.

A microresonator laser frequency comb in the mode-locked state is generated via the dual-driven pump approach, with a larger intracavity dispersion of -150.8 $fs^2$/mm. We characterize the timing jitter with the self-heterodyne linear interferometer (SHLI), and subsequently compare with the original close-to-zero intracavity dispersion (path averaged GVD to -4.39 $fs^2$/mm) mode-locked frequency microcomb. This is illustrated in Figure S2. Figure S2a and S2b show the measured cavity group velocity dispersion and the soliton microcomb optical spectrum. We observed that this larger dispersion microresonator increases the timing jitter to 14.37 fs integrated from 100 kHz to 10 kHz compared to our demonstration of the close-to-zero dispersion low-jitter state of 1.7 ± 0.7 fs as shown in Figure S2c. The Fourier frequency bandwidth of the measured timing jitter PSD is determined by our FFT analyzer bandwidth (SR 770 FFT Network Analyzer).

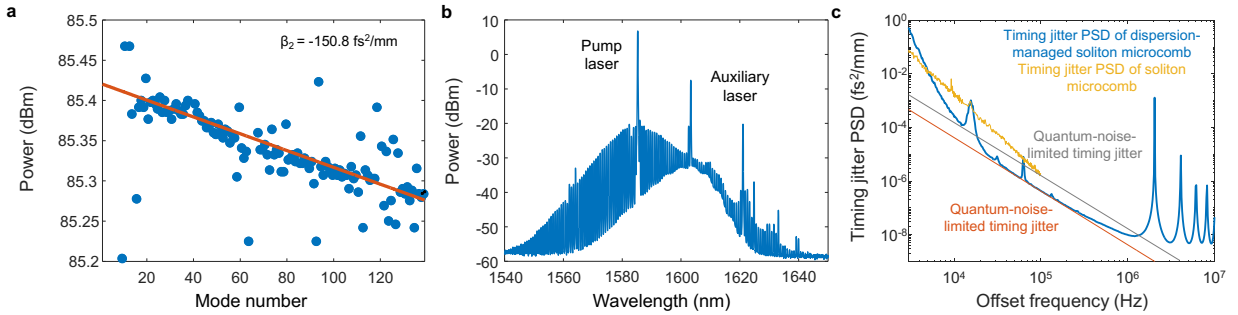


**Figure S2 | Self-heterodyne linear interferometry measurement of timing jitter in the mode-locked soliton frequency microcomb, with larger intracavity dispersion in comparison with**

**close-to-zero dispersion microresonator. a,** Measured cavity group velocity dispersion. **b,** Measured soliton microcomb optical spectrum. **c,** Measured timing jitter power spectral density.

Then, the pump laser intensity noise is characterized to illustrate the influence from electrical noise, EDFA noise, and free-space-to-chip coupling noise as shown in Figure S3. Measurements are conducted before the microresonator, after the microresonator when on and off resonance, and without the EDFA and are compared against the detector and instrumentation noise floor. From the RIN measurements, the free-space-to-chip coupling fluctuations below ≈ 7 kHz can be observed with additional intensity noise degradation. After the pump wavelength is tuned into the resonance, the extra coupling noise below 1 kHz is observed as well.

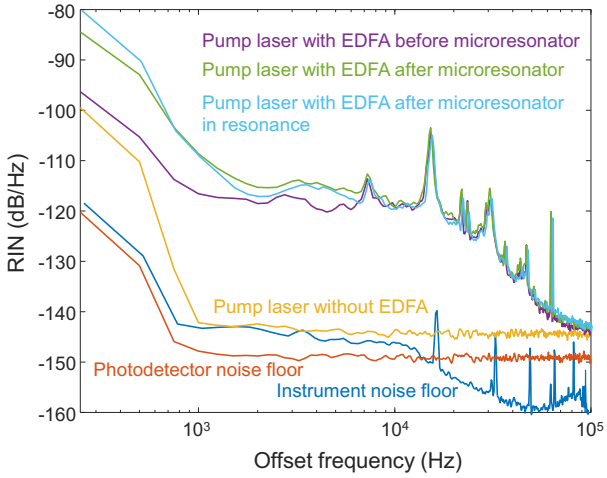


**Figure S3 | The measured relative intensity noise (RIN) of the pump laser.**

## II. Characterizing the self-heterodyne linear interferometer frequency discrimination sensitivity and timing jitter measurement resolution

The fiber-delay-lined-based phase noise measurement is an averaged measurement [34,48,63,64]. The photodetected signal of each mode is filtered at $f_{aom}$ and mixed by an RF mixer to reject the common-mode $f_{ceo}$ noise. This downconverted RF mixer output contains the repetition-rate phase noise or timing jitter as a form of $\delta[\tau(m - n)f_{rep}]$. The frequency fluctuations of the two selected optical comb lines are converted into voltage fluctuations with the transfer function $\Delta V(f) \propto K_{\varphi} \frac{|1-e^{-i2\pi f\tau}|}{|i\times f|}(m-n)\Delta f_R(f)$ where $K_{\varphi}$ is the peak voltage at the double-balanced mixer output. In our manuscript, we used 49-meter fiber for the timing jitter power spectral density measurement in the fiber Michelson interferometer which is noted in Figure 4 caption and Methods. The time delay is around 0.49 μs corresponding to Fourier frequency of 2.04 MHz. This Fourier

frequency set the upper offset frequency bound for our measurement. For the self-heterodyne linear interferometry timing jitter measurement technique, the heterodyne beat note, frequency discrimination calibration and the measured frequency noise are illustrated in Figure S4. The heterodyne detection beat note magnitude and delay time determines the frequency discrimination sensitivity via: $\Delta V(f)/\Delta f_R(f) \propto K_\varphi \frac{|1-e^{-i2\pi f\tau}|}{|i\times f|}(m-n)$.

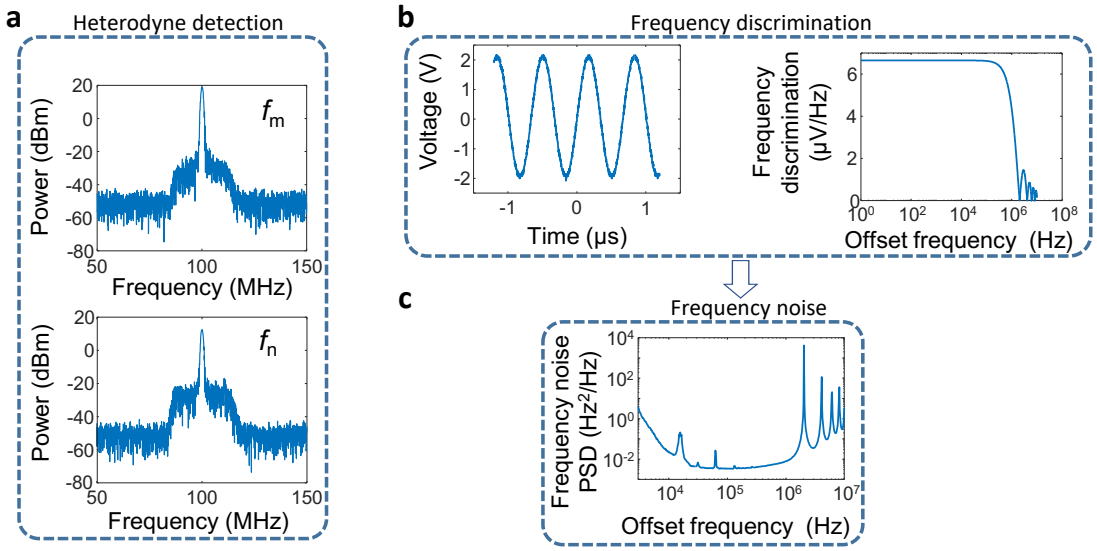


**Figure S4 | Frequency discrimination and timing jitter measurement calibration. a,** Example measured heterodyne beat note at the 100 MHz frequency. **b,** Frequency discrimination calibration of the system at 6.75 μV/Hz from 1 to 100-kHz offset. **c,** Measured frequency noise power spectral density of 3-$Hz^2$/Hz at 3-kHz offset and $3\times10^{-3}$ $Hz^2$/Hz at 100-kHz offset.

To characterize the system sensitivity, we carried out the experiment by setting $m = n$, wherein the noise floor is determined after common-mode noise rejection. The measured timing jitter measurement sensitivity is illustrated in Figure S5 where we set the delay time to $\tau$ = 489 ns, 742 ns, and 1.24 μs. First, we calibrate the timing jitter sensitivity as shown in Figure S5a which shows the timing jitter power spectral density noise floor of $1.6 \times 10^{-10}$ $fs^2$/Hz. Over the same integrated frequency range of the timing jitter power spectral density, the integrated timing jitter is less than 0.1 fs. The system sensitivity calibration of sub-fs timing resolution shows the self-heterodyne linear interferometry could enable the femtosecond timing jitter characterization.

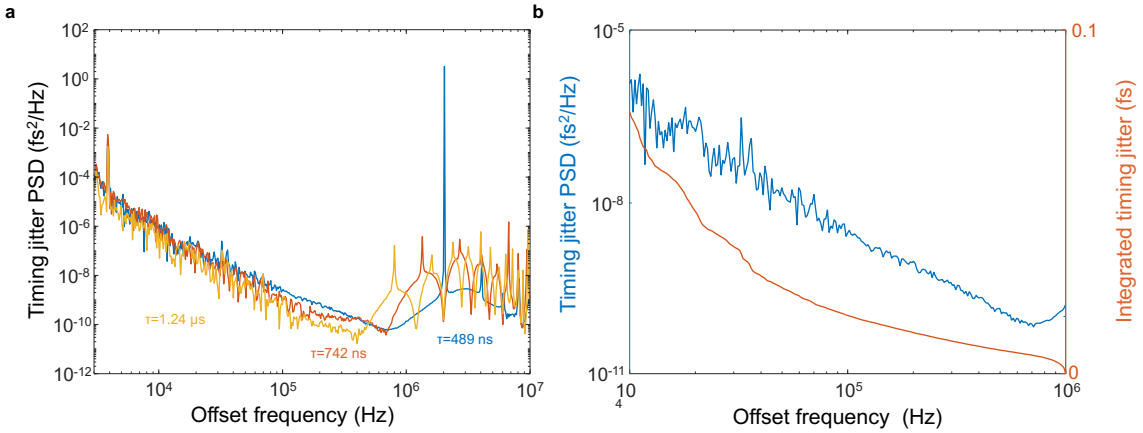


**Figure S5 | The timing jitter measurement sensitivity. a,** The determined timing jitter measurement sensitivity with different delay times. **b,** The determined timing jitter power spectral density and integrated timing jitter of the self-heterodyne linear interferometer noise floor.

**III. Representative timing jitter and relative intensity noise performances of free-running mode-locked lasers.**

Table S1 below summarizes the comparison of timing jitter in representative free-running mode-locked lasers. An example of applications enabled by the jitter-power tradeoffs can be seen in Ref. [68]. The chip-scale frequency microcombs provide a small size, weight, power and robustness compared to bulk mode-locked lasers. A low relative intensity noise is also helpful for applications in communications, and sensing. For example, a -153-dB/Hz would help in applications of optical communication for data processing. Most semiconductor diode lasers are in the range of -150 dB/Hz to -170 dB/Hz [69]. This is illustrated in Table S2 below.

**Table S1 | Example jitter comparison of free-running mode-locked lasers.**

| Solid-state Laser /Fiber/ Microcavity | Timing jitter PSD at 10 kHz ($fs^2$/Hz) | Integrated timing jitter (fs) | Integrated Fourier frequency range | Measurement method |
|---|---|---|---|---|
| 500 MHz, SESAM, Er:Yb-glass laser [65] | $7\times10^{-8}$ | 0.016 | [10 kHz - 250 MHz] | OH[a] |
| 80 MHz, CNT-SA, soliton Er-fiber laser [66] | $3\times10^{-5}$ | 0.5 | [10 kHz - 40 MHz] | BOC[a] |
| 80 MHz, NPR, soliton Yb-fiber laser [67] | $6\times10^{-4}$ | 1.8 | [10 kHz - 40 MHz] | BOC |
| 20 GHz Silicon nitride frequency microcomb [12] | $7\times10^{-3}$ | | | High-speed detector |
| 22 GHz silica microcombs [35] | $1\times10^{-3}$ | 2.6 | [10 kHz - 3 MHz] | FI[c] |
| 22 GHz silica microcombs [44] | $1\times10^{-4}$ | – | – | BOC |
| **89 GHz, dual-driven, soliton nitride microcomb [this work]** | $3\times10^{-4}$ | 1.7 | [10 kHz - 1 MHz] | SHLI |

BOC: Balanced optical cross-correlation; OH: optical heterodyne; FI: fiber interferometer; SHLI: self-heterodyne linear interferometer.

**Table S2 | Example RIN comparison of free-running mode-locked lasers.**

| Example laser frequency comb system | Relative intensity noise [dB/Hz] at 1 kHz offset frequency | Relative intensity noise [dB/Hz] at 1 MHz offset frequency |
|---|---|---|
| 500 MHz, SESAM, Er:Yb-glass laser [70] | -110 | -140 |
| 1 GHz, SESAMa, soliton Yb:CALGO laser [71] | -115 | -145 |
| 194 MHz, NPRa, soliton Er-fiber laser [72] | -140 | -145 |
| **89 GHz, dual-driven, soliton nitride microcomb [this work]** | -118 | - 153 |